CARBON 85 (2015) 60–71

Available at www.sciencedirect.com

ScienceDirect

journal homepage: www.elsevier.com/locate/carbon

N-doped carbon layer coated thermally exfoliated graphene and its capacitive behavior in redox active electrolyte

Yinan Yan [a,b], Tapas Kuila [c,*], Nam Hoon Kim [a], Seung Hee Lee [a,d], Joong Hee Lee [a,d,*]

[a] Advanced Materials Research Institute for BIN Fusion Technology & Department of BIN Fusion Technology, Chonbuk National University, Jeonju, Jeonbuk 561-756, Republic of Korea

[b] National Engineering Research Center for Nanotechnology, Shanghai 200241, PR China

[c] Surface Engineering & Tribology Division, CSIR-Central Mechanical Engineering Research Institute, Council of Scientific & Industrial Research (CSIR), Mahatma Gandhi Avenue, Durgapur 713209, India

[d] Carbon Composite Research Center and Department of Polymer & Nano Engineering, Chonbuk National University, Jeonju, Jeonbuk 561-756, Republic of Korea

ARTICLE INFO

Article history:
Received 8 October 2014
Accepted 19 December 2014
Available online 24 December 2014

ABSTRACT

A nitrogen-doped carbon layer coated thermally exfoliated graphene (NC-TEG) is prepared by in-situ polymerization of p-phenylene diamine (PD) with thermally exfoliated graphene (TEG) and subsequent high temperature pyrolysis (600 °C for 1 h in argon gas environment). Fourier transfer infrared spectroscopy, X-ray photoelectron spectroscopy, and scanning electron microscopy confirm the formation of poly-(p-phenylene diamine) layers on the TEG surfaces with a nitrogen doping level of ~6.1%. Physisorption analysis indicates that NC-TEG not only has the enlarged surface area, but also forms hierarchical three dimensional structures with several micro and meso-pores compared to pristine TEG. Due to the synergic effect of nitrogen atoms in the carbon structures and augmented surface area, the capacitance measured from cyclic voltammetry and galvanic charge–discharge increases to 282.5 F g^{-1} from the 95.1 F g^{-1} of TEG. Moreover, the PD monomer acts as a reversible faradaic agent. The capacitive performance of the NC-TEG electrode is investigated in different mixed electrolytes. The specific capacitance is significantly increased to 635.6 F g^{-1} in a mixed electrolyte of 0.025 M PD and 2 M KOH. After 10,000 cycles, the capacitive retention shows remarkable stability as high as 87.4%.

1. Introduction

Porous conductive materials with a large surface area and high electrochemical stability are preferable for the fabrication of energy storage electrodes [1]. Particularly, carbon materials such as activated carbon, fullerene, carbon onion, carbon nanotube, carbon fibers, and other carbonaceous materials can be prepared by the pyrolysis of resins [2–8]. These carbonaceous materials are appealing to address the demands of energy storage devices to allow the fabrication of electric

* *Corresponding authors at:* Advanced Materials Research Institute for BIN Fusion Technology & Department of BIN Fusion Technology, Chonbuk National University, Jeonju, Jeonbuk 561-756, Republic of Korea. Fax: +82 63 270 2341 (J.H. Lee).
E-mail addresses: jhl@chonbuk.ac.kr (J.H. Lee), tkuila@gmail.com (T. Kuila).
http://dx.doi.org/10.1016/j.carbon.2014.12.069
0008-6223/

double layer (EDL)-type supercapacitors for the storage of electrical energy, which is induced by physical separation of charge in Helmholtz double layer at the interface between electrode and electrolyte [9]. The electrical double layer capacitor (EDLC) is noted for high power density, fast charge–discharge rates and lengthy cycle life. Graphene, as a novel isotope material in the carbon family, has drawn worldwide attention for its colossal surface area and its crystalline structure prompting electron transfer and increased electron mobility [10]. As one species of thin graphene flakes, thermally exfoliated graphene (TEG) sheets can be synthesized by the exfoliation of graphite oxide at high temperature, have the advantages of good mechanical integrity, excellent conductivity and high electrolyte-accessible porous surface area, and have become a promising material in the design of supercapacitor electrodes [11–12].

With the intention to improve supercapacitive performance, attempts have been made to increase surface area through the exfoliation of graphite oxide under vacuum [13–14] and post-treatment of graphene for activation [15]. However, due to the hydrophobic nature of carbon material, the specific capacitance improvements achieved through the above-mentioned approaches are all limited to less than 220 F g^{-1}. Nevertheless, heteroatom doping (nitrogen, boron [16], or sulfur [17]) on a carbon framework exhibits effective improvement by resolving the problems such as ameliorating rinse and increasing reactivity of carbon electrodes. Nitrogen doping can be achieved either through post-treatment with small molecular agents such as, urea [18] and ammonia gas [19] or via carbonization of nitrogen-rich polymer precursors, like polyacrylonitrile [20], methylated melamine resin [21], and polypyrroles [22]. Comparatively, the methods using post-treatment often resulted in the detachment of unstable functional groups, which seriously reduces the capacitive performance after multiple charge–discharge cycles. In contrast, the carbonization of nitrogen-rich polymer precursors efficiently promotes stable hetero nitrogen atom incorporation into carbon skeletons. Moreover, pseudo-capacitive behavior resulting from reversible faradic electron-transfer chemical reactions is expected to associate EDLC and exhibit synergistic enhancement of specific capacitance. Various valence reversible material/carbon composites [23–25] were developed as supercapacitor electrodes. Specially, a faradaic pseudo-capacitive contribution based on the rapid redox processes of a mediator in electrolyte has been extensively investigated. Addition of Indigo carmine [26], hydroquinone [27], potassium ferricyanide [28], methylene blue [29], lingo sulfonates [30] or benzenediol [31] in acid electrolyte and mixing potassium iodine and bromide [32] in the alkali electrolyte have been reported to augment capacitive performances.

P-phenylene diamine (PD) has been broadly used in electrochemical reactions as an enhanced mediator to facilitate electron transitions in bio-sensors and catalyst [33–34]. Herein, we report for the first time the application of redox-active electrolyte on TEG materials. Different from previous studies, PD herein was polymerized with TEG as the pyrolysis precursor for preparing higher surface NC-TEG. The as-made materials were characterized in terms of surface area, chemical composition, morphology, and electrochemical performance. Moreover, the intrinsic reversible chemical structure alteration between PD and p-phenylene diimine (mechanism shown in Fig. 1) intensifies the electron transfer in the midst of NC-TEG electrode and KOH electrolyte, leading to a direct increase in capacitive performance [35]. The combination of redox pseudo-capacitive electrolyte mediator and the EDL effective electrodes induced a synergic capacitive increase in the charge-discharge process.

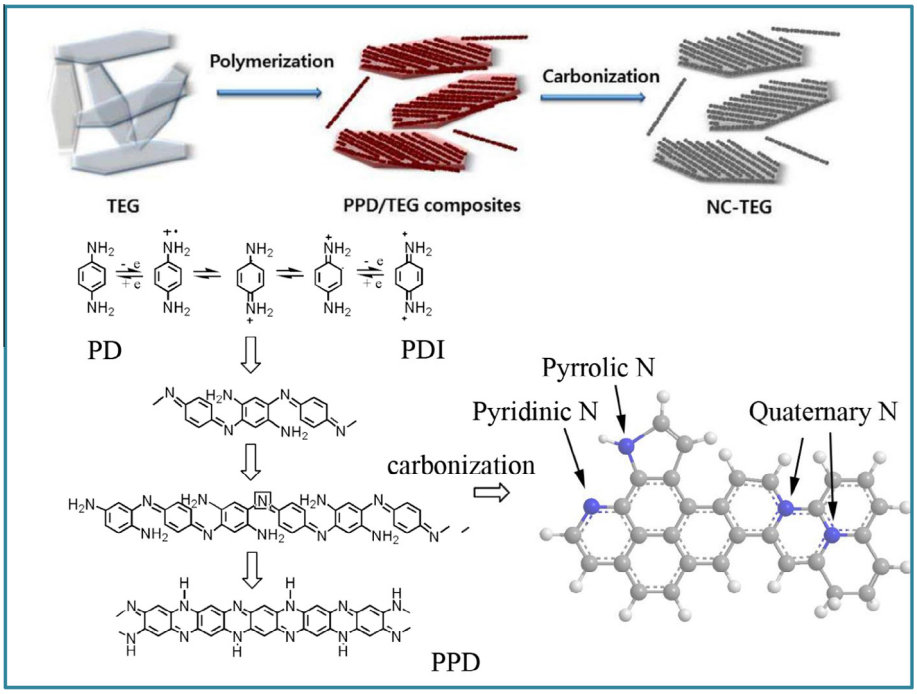

Fig. 1 – Schematic of the preparation of NC-TEG. (A colour version of this figure can be viewed online.)

2. Experimental

2.1. Materials

Expanded graphite (TIMREX®BNB90, specific surface area of 28.4 $m^2 g^{-1}$) was purchased from TIMCAL Co., Ltd., USA. Sulfuric acid, hydrochloric acid, ethanol, and hydrogen peroxide were purchased from Samchun Pure Chemical Co., Ltd., Korea. Potassium permanganate, used as an oxidization agent was purchased from Junsei Chemical Co., Ltd., Japan. N-methyl pyrrolidone (NMP) was purchased from Sigma Aldrich and was used as a solvent without further purification. PD as monomer and electrolyte mediator was purchased from Sigma Aldrich Co., Ltd. Cetrimonium bromide (CTAB), used as a stabilizer, was purchased from Sigma Aldrich. Ammonium persulfate (APS) served as a polymerization catalyst to synthesis poly-(p-phenylene diamine) (PPD) was purchased from TCI, Japan.

2.2. Preparation of TEG

Graphite oxide was prepared by modified Hummer method, and the as-made graphite oxide was dried at 60 °C under vacuum. Dried graphite oxide papers were pulverized into powders by a household blending machine and stored in a sealed ampoule to prevent moisture contamination. Approximately 0.1 g of pre-dried graphite oxide powder was placed in a nickel-metal crucible pre-charged with argon (99.99% argon gas) and was then placed in a preheated muffle furnace at 1000 °C for ~30 s. The resultant TEG samples were stored in sealed ampoules.

2.3. Preparation of PPD-TEG composite and NC-TEG

Emulsion polymerization was carried out to achieve coating. The stabilizer, CTAB was mixed with 30 mg of TEG powder in 150 ml of deionized (DI) water to obtain a stable micelle dispersion. The PD water dispersion was dripped into the micelle solution and stirred for 2 h. Approximately 1 g of APS, dissolved in 30 ml DI water as an oxidant and catalyst, was slowly dripped into the previous micelle solution, and the reacting temperature was controlled between 0 and 5 °C. The product precipitated after 24 h of reaction and was washed by filtering with a large quantity of DI water – ethanol mixture to remove excess CTAB followed by drying in the oven for 24 h at 80 °C. The as-prepared composites were placed in a Lindberg furnace, and the temperature was increased to 600 °C with the rate of 5 °C min^{-1}. The sample was annealed for 1 h (pre-charged with 99.99% argon gas, with a flow speed of 30 ml min^{-1}) followed by cooling to room temperature. The as-prepared sample was sealed in ampoules for storage.

2.4. Preparation of electrodes and electrolytes

TEG, PPD-TEG, and NC-TEG were made into slurries with 5% PVDF as a binder and NMP as the solvent. The slurries were drop-casted onto a nickel foam electrode within an area of 1 cm^2. TEG, PPD-TEG, and NC-TEG electrodes were placed under vacuum at 70 °C for ~48 h to remove excess NMP. Different concentrations of KOH (1, 2, 4, or 6 M) electrolyte were used for the electrochemical testing. The mixed electrolyte was prepared by mixing PD and KOH in 5 ml DI water. The compositions of the various electrolytes are shown in Table 1.

Table 1 – Compositions of various mixed electrolytes.

Sample	Amount of water (ml)	Amount of KOH (g)	Concentration of PD (M)	Amount of PD (g)
PK11	5	0.28	0.000	0
PK12	5	0.28	0.010	0.0054
PK13	5	0.28	0.025	0.0135
PK14	5	0.28	0.050	0.027
PK15	5	0.28	0.100	0.054
PK21	5	0.56	0.000	0
PK22	5	0.56	0.010	0.0054
PK23	5	0.56	0.025	0.0135
PK24	5	0.56	0.050	0.027
PK25	5	0.56	0.100	0.054
PK31	5	1.12	0.000	0
PK32	5	1.12	0.010	0.0054
PK33	5	1.12	0.025	0.0135
PK34	5	1.12	0.050	0.027
PK35	5	1.12	0.100	0.054
PK31	5	1.68	0.000	0
PK32	5	1.68	0.010	0.0054
PK33	5	1.68	0.025	0.0135
PK34	5	1.68	0.050	0.027
PK35	5	1.68	0.100	0.054

2.5. Characterization

Fourier transform infrared (FT-IR) spectroscopy of TEG, PPD-TEG, and NC-TEG samples was carried out using a FT-IR 4100 spectrometer (Jasco Instrumental, Japan) at room temperature in the frequency range of 4000–400 cm^{-1}. Thermogravimetric analysis (TGA) was performed in a nitrogen atmosphere using a Q50 TGA system (TA Instruments, USA), in the temperature range of 40–700 °C at a heating rate of 5 °C min^{-1}. Raman spectra were obtained on a Nanofinder 30 (Tokyo Instruments Co., Osaka, Japan). X-ray photoelectron spectroscopy (XPS) was performed on an AXIS-NOVA analysis system (Kratos Analytical Ltd., UK) with the following parameters: Al-Kα = 1486.6 eV, power = 150 W (HV = 15 kV and I = 10 mA). The XPS were calibrated for both beam intensity and charging (reference the binding energy at 284.4 eV of the C1s peak). Prior to fitting, the Shirley background was subtracted. Peak areas were normalized with theoretical cross-sections to obtain the relative surface elemental compositions. Elemental analysis was carried out at Vario EL cube, (Elementar, Germany) for the determination of the C, N, and O contents. The isotherm of nitrogen physical-adsorption was obtained using an ASAP-2020 surface analyzer (Micromeritics Instruments, USA), and the specific surface area (SSA) was determined by the Brunauer–Emmett–Teller (BET) method. The SSA of the micro-pores was calculated via the Barrett–Joyner–Halenda adsorption (BJH) approach. Morphology was characterized using a JSM-6701F field emission scanning electron microscope (FE-SEM) (JEOL Instruments, Japan) operated at 2.0 kV. High-resolution transmission electron

microscopy (HR-TEM) measurements were carried out using an H-7650 (Hitachi, Japan) microscope operated at 120 kV. Samples for TEM measurements were prepared by dispersing TEG, PPD-TEG, and NC-TEG in NMP at a concentration of 0.2 mg ml^{-1}. Then, 5 μL aliquots of these samples were drop-casted onto carbon-coated copper grid. Electrochemical properties of TEG and NC-TEG samples were measured with a CH660D electrochemical work station system (Chenhua Instruments, China). The measurements were carried out in an aqueous system. A platinum foil was utilized as the counter electrode, and a reversible Ag/AgCl solution was the reference electrode. The specific capacitance was determined from galvanostatic charge-discharge using the equation, specific capacitance = $(I \times \Delta t)/(m \times \Delta V)$, where I is the galvanic current (A g^{-1}), m is the mass of active material (mg), Δt is the charge–discharge time (sec), and ΔV is the potential window (V). Coulombic efficiency was calculated using the equation, Coulombic efficiency = (discharging time/charging time) × 100.

3. Results and discussion

3.1. FT-IR spectra analysis

FT-IR spectra of TEG, PPD-TEG, and NC-TEG samples are shown in Fig. 2. The decreased peak intensities of oxygen functionalities at 3440 (–OH stretching vibration), 1720 (–COOH stretching), 1209 (C–O, epoxy stretching), and 1057 cm^{-1} (C–O, alkoxy stretching) in the TEG confirmed the partial removal of oxygen functional groups during thermal treatment at 1000 °C. The bands at 2927 and 2854 cm^{-1} were designated as the C–H stretching and vibration of the $–CH_2–$ groups, respectively [36]. For PPD-TEG, the typical peaks at 3316 and 3200 cm^{-1} denote the amine group stretching vibrations of –NH– and $–NH_2–$ groups, respectively, thereby confirming the existence of nitrogen elements in the as-prepared PPD-TEG composite. The peaks centered at 1611 and 1509 cm^{-1} were ascribed to the —C=C— stretching vibrations of quinonoid and benzenoid rings, respectively. The peaks at 1394 and 1305 cm^{-1} were respectively assigned to the –C–N– stretching of the imine units of quinonoid and benzenoid structures. Peaks at 1041, 837, and 749 cm^{-1} suggested the existence of substituted benzene ring C–H bending vibrations and out-of-plane vibrations [37]. The above observation indicated that the PPD component was coated on the surface of TEG by π–π interactions between the aromatic structure of PPD polymer and the honeycomb rings of graphene. Interestingly, the out-of-plane deformation peaks for C–H vibrations at 837 and 749 cm^{-1} disappeared upon annealing of PPD at 600 °C for 1 h, suggesting dehydrogenation and formation of a highly conjugated structure. The remaining two peaks at 1631 and 1391 cm^{-1} denote the quinonoid and benzenoid ring structure in the N-doped carbon composite, respectively.

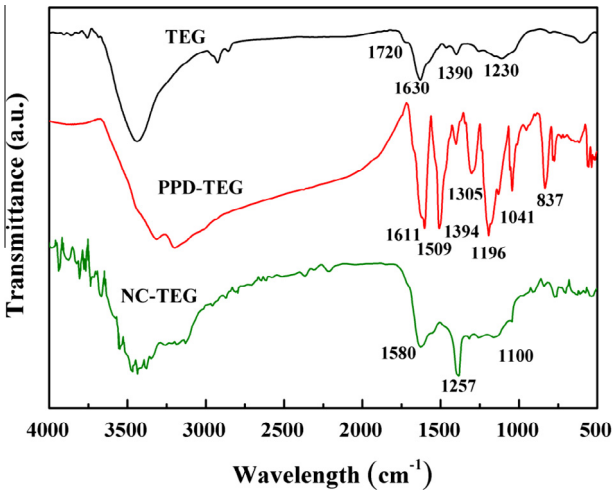

Fig. 2 – FT-IR spectra of TEG, PPD-TEG, and NC-TEG. (A colour version of this figure can be viewed online.)

3.2. TG analysis

TG analysis was performed to investigate the thermal stability of TEG, PPD-TEG and NC-TEG as shown in Fig. 3. The thermogram obtained for TEG showed good stability without weight loss below 300 °C, and ~6.12% weight loss was observed between 300 and 800 °C due to the pyrolysis of oxygen-containing functional groups, such as hydroxyl and carboxyl groups. In the case of PPD-TEG composites, an approximate 2.37% weight loss below 100 °C was recorded, corresponding to the evaporation of adsorbed moisture. A 7.18% weight loss was observed between 100 and 400 °C, which was due to the decomposition of PPD oligomers. The carbonization process from 400 to 800 °C resulted in a ~8.1% weight loss due to the further loss of edge functional nitrogen elements. The carbonization temperature was fixed at 600 °C, leading to the formation of ~81.5% residue for the electrodes [38]. The thermograms clearly demonstrated that the thermal stability of NC-TEG was higher than that of TEG or PPD-TEG due to the doping of nitrogen atoms in the honeycomb skeleton of the graphene structure.

3.3. Raman spectra analysis

Carbonization of PPD-TEG at 600 °C in an argon environment was also investigated through Raman spectroscopic analysis. Raman spectra obtained for TEG, PPD-TEG, and NC-TEG are shown in Fig. 4. For TEG, two apparent bands were observed at 1350 and at 1580 cm^{-1}, corresponding to the disorder-induced D band and crystalline graphitic G band, respectively. The intensity ratio of D to G bands (I_D/I_G) was found to be 1.29. The Raman spectrum of PPD-TEG demonstrated numerous peaks associated with short oligomers of aniline, the structures potentially containing phenazine-like and benzoquinone structures. After heating to 600 °C within one hour, two broad bands located at 1580 and 1340 cm^{-1} were observed. These bands can be considered as G-band ("graphitic" band, stretching of any pair of sp^2 carbons) and D-band ("disorder" band, breakage of hexagonal carbon rings activated by any defect included by a heteroatom). These bands are defined for graphitic material and proved to be applicable for a nitrogen-containing analogue, and the I_D/I_G ratio of NC-TEG was 1.13. The spectrum corresponds to the disordered nitrogen-containing graphitic material.

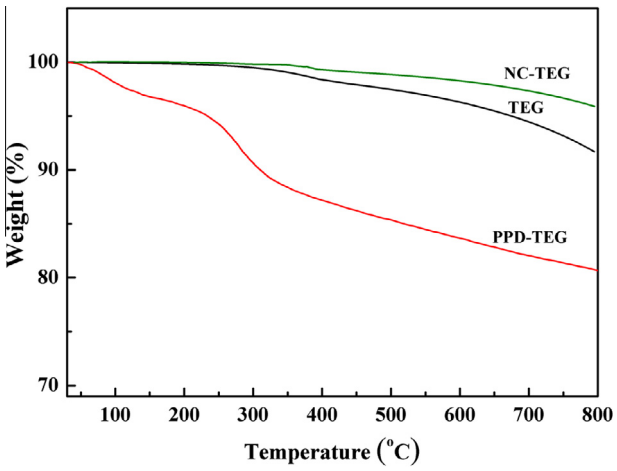

Fig. 3 – TG analysis of TEG, PPD-TEG, and NC-TEG. (A colour version of this figure can be viewed online.)

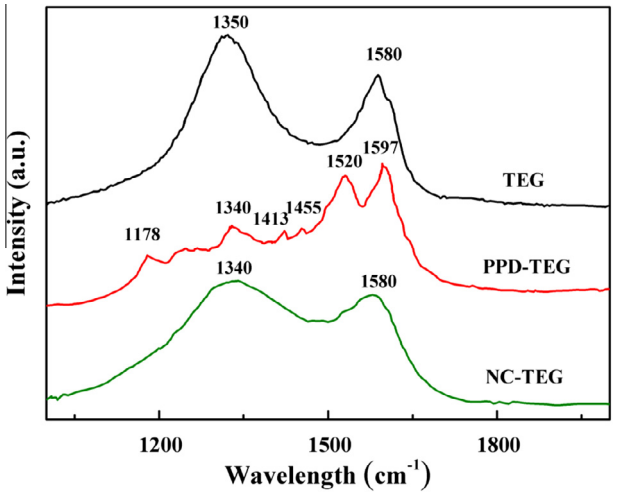

Fig. 4 – Raman spectra of TEG, PPD-TEG, and NC-TEG. (A colour version of this figure can be viewed online.)

3.4. *Physisorption analysis*

Surface areas and pore-size distributions of TEG, PPD-TEG and NC-TEG samples were investigated using nitrogen adsorption–desorption tests. H3-type hysteresis loops were observed in the adsorption and desorption curves of TEG and O-TEGs (Fig. 5(a)), and are similar to those observed in nano-clays and nano-structured materials with slits. The shape of the adsorption–desorption curve was narrow and moon-like and different from the flat-slit shape observed for activated carbon, without the presence of either H1- or H2-type hysteresis loops. The surface area of TEG reached 400 $m^2 g^{-1}$. However, the loops of PPD-TEG and NC-TEG were completely changed. The measured surface areas of PPD-TEG and NC-TEG were about 59.2 and 650 $m^2 g^{-1}$, respectively. This increase in surface area after pyrolysis is consistent with the reported literature [39]. Correspondingly, the carbonization process of PPD was investigated by Tomas Plachy and colleagues; they reported that the surface areas of annealed polymers increased by ten-fold compared those of its

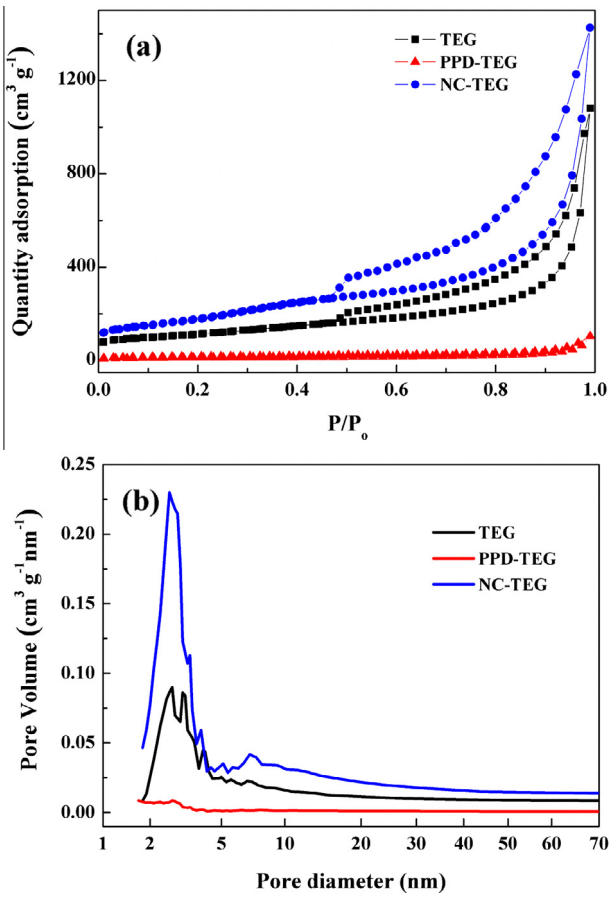

Fig. 5 – (a) Adsorption and desorption curves of TEG, PPD-TEG, and NC-TEG and (b) the pore distribution of TEG, PPD-TEG and NC-TEG. (A colour version of this figure can be viewed online.)

precursors. The pore-size distributions of TEG, PPD-TEG, and NC-TEG are presented in Fig. 5(b). In comparison to TEG, PPD-TEG showed a limited pore volume due to the thick polymer coating layers. However, NC-TEG showed a prominent volume increase in the milli- and meso-pore range of 2–5 and 5–70 nm, respectively, which is attributed to the carbonization of PPD polymers.

3.5. *XPS analysis*

XPS analysis was carried out to determine the exact amount of functional component. Complete spectrums of TEG, PPD-TEG, and NC-TEG are shown in Fig. 6(a). The atomic elemental percentages of carbon, nitrogen, and oxygen deconvolution are summarized in Table 2. In comparison to TEG, the intensities of oxygen functionalities were decreased and those of nitrogen functionalities were increased in PPD-TEG, reflecting the change in chemical composition. The C1s spectrum of TEG shown in Fig. 6(b) was deconvoluted into five main peaks. The peaks at 284.6, 286.1, 288.1, 289.1, and 291.2 eV were assigned to —C—C—/—C=C—, C—O—C/C—OH, —C=O, —COOH, and π-plasmon generated from π–π^* shake-up transitions, respectively. The existence of a 291.2 eV peak illustrated the abundance of aromatic ring structures in the TEG sample.

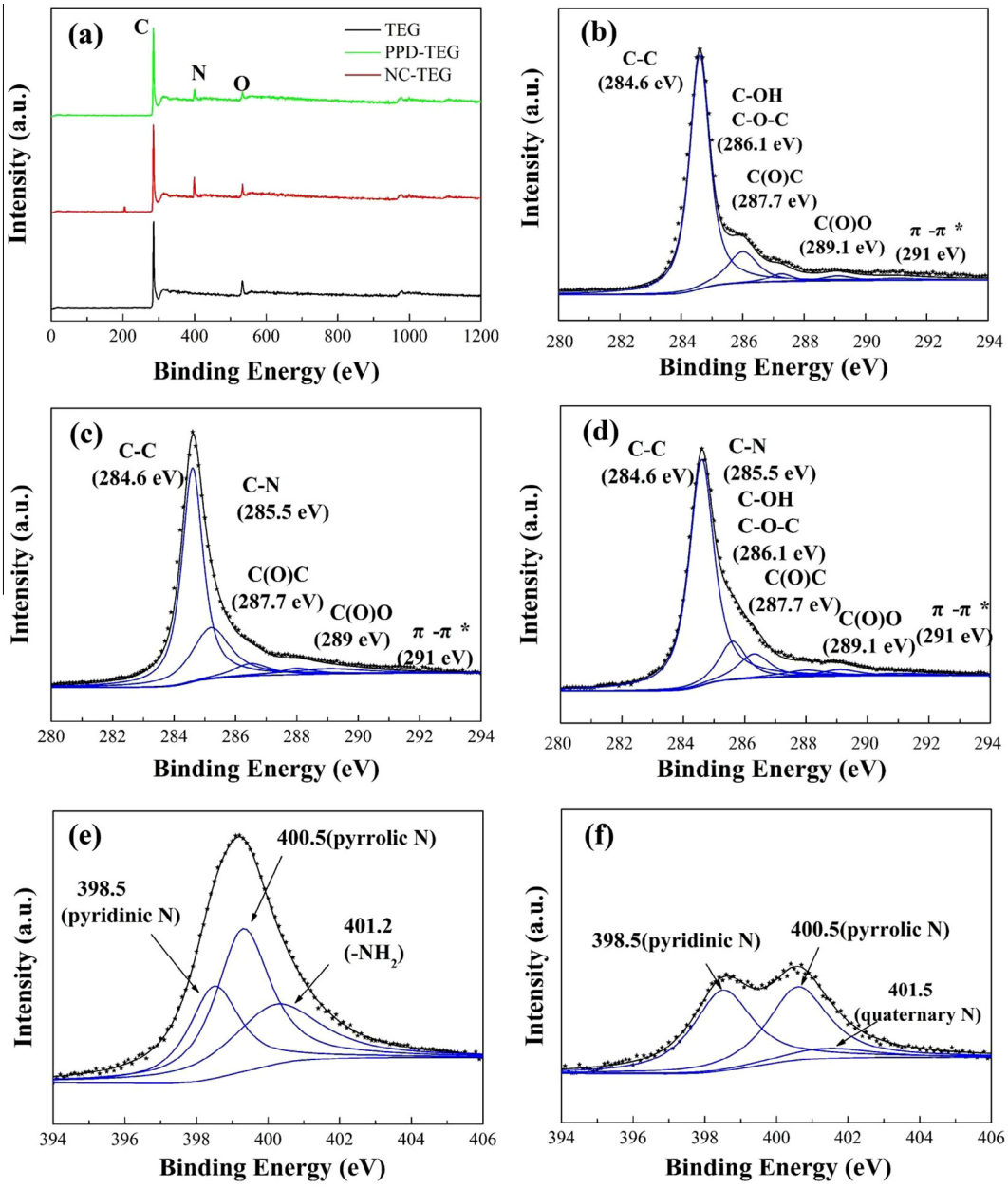

Fig. 6 – (a) XPS spectra survey of TEG, PPD-TEG, and NC-TEG, C1s spectra of (b) TEG, (c) PPD-TEG, (d) NC-TEG, and N1s spectra of (e) PPD-TEG and (f) NC-TEG. (A colour version of this figure can be viewed online.)

The C1s deconvoluted spectrum of PPD-TEG is shown in Fig. 6(c). In comparison to TEG, there is no trace of a π-plasmon peak in the PPD-TEG. However, the appearance of a new peak at 285.6 eV reflects the bonding between carbon and nitrogen atoms as —C—NH— or —C=N— confirming the successful coating of PD onto the TEG. The C1s deconvoluted spectrum of NC-TEG (Fig. 6(d)) exhibited decreased intensity of —C—NH—, —C—O, and —C=O due to the pyrolysis of samples during annealing at 600 °C.

The transformation of PPD during pyrolysis was reflected in the N1s spectrum of XPS measurements. As shown in Fig. 6(e), the N1s of PPD-TEG composite was deconvoluted into three components: pyridinic N at 398.5 eV, imino N at 399.3 eV, and amino N at 400.2 eV. In the composite, imino and amino N were the main component groups. Pyridinic rings were formed through polymerization under the oxidation effect of ammonium persulfate. After pyrolysis under an inert atmosphere, a new peak appeared at 401.5 eV, which is designated as quaternary N, and at the same time, the intensities of pyridinic and pyrrolic N were decreased due to carbonization [31]. This observation was strongly supported by the XPS elemental analysis results as shown in Table 3. It shows that the N content (~16.2%) in PPD-G was decreased to 6.1% in NC-TEG.

3.6. *FE-SEM image analysis*

Scanning electron microscopy characterization was performed, and the images of TEG, PPD-TEG, and NC-TEG are presented in Fig. 7(a–d). Numerous exfoliated TEG flakes are

Table 2 – XPS elemental analysis of TEG, PPD-TEG, and NC-TEG.

B.E. (EV)	C1 (284.6)	C2 (285.6)	C3 (286.1)	C4 (277.7)	C5 (289.1)	C6 (291.1)	N1 (398.5)	N2 (400.5)	N3 (401.2)	N4 (401.5)
TEG	76.88	0	15.67	3.02	2.75	1.38	0	0	0	0
PPD-TEG	56.42	32.08	6.09	3.15	2.26	0	25.12	44.81	30.07	0
NC-TEG	59.33	18.85	15.52	2.89	2.14	1.27	47.63	43.55	0	8.82

Table 3 – XPS elemental analysis results for TEG, PPD-G and NC-TEG.

Sample	C (At. wt%)	O (At. wt%)	N (At. wt%)
TEG	89.8	9.1	0
PPD-G	72.2	6.9	16.2
NC-TEG	84.9	8.3	6.1

shown in Fig. 7(a) and the high-resolution image is presented in Fig. 7(b). Defected holes were observed on the surface of graphene, due to the burn-down process of graphite oxide defect zones. Crumpled graphene sheets randomly aggregated and associated with each other, presenting a highly disordered solid form indicating the presence of curved and coiled edges of graphene sheets. The formation of a three-dimensional highly crystalline honeycomb-like structure with massive pores was identified through the edges of crumpled sheets. These crumpled TEG sheets were able to prevent restacking between layers when they were compressed into electrodes. The morphology of the PPD-TEG composite is shown in Fig. 7(c–d). It is observed that the thickness of individual PPD-TEG sheets increased to 20–40 nm. In comparison to TEG, the original cavity between overlapped TEG flakes disappeared, and the spaces were filled with amorphous polymer material after coating. Nano-size PPD granules were grown on the surface of TEG, which is perturbed by self-nucleation; a similar result has been reported in polyaniline-coated graphene materials [40]. An image of NC-TEG is shown in Fig. 7(e) and (f). After incineration treatment with

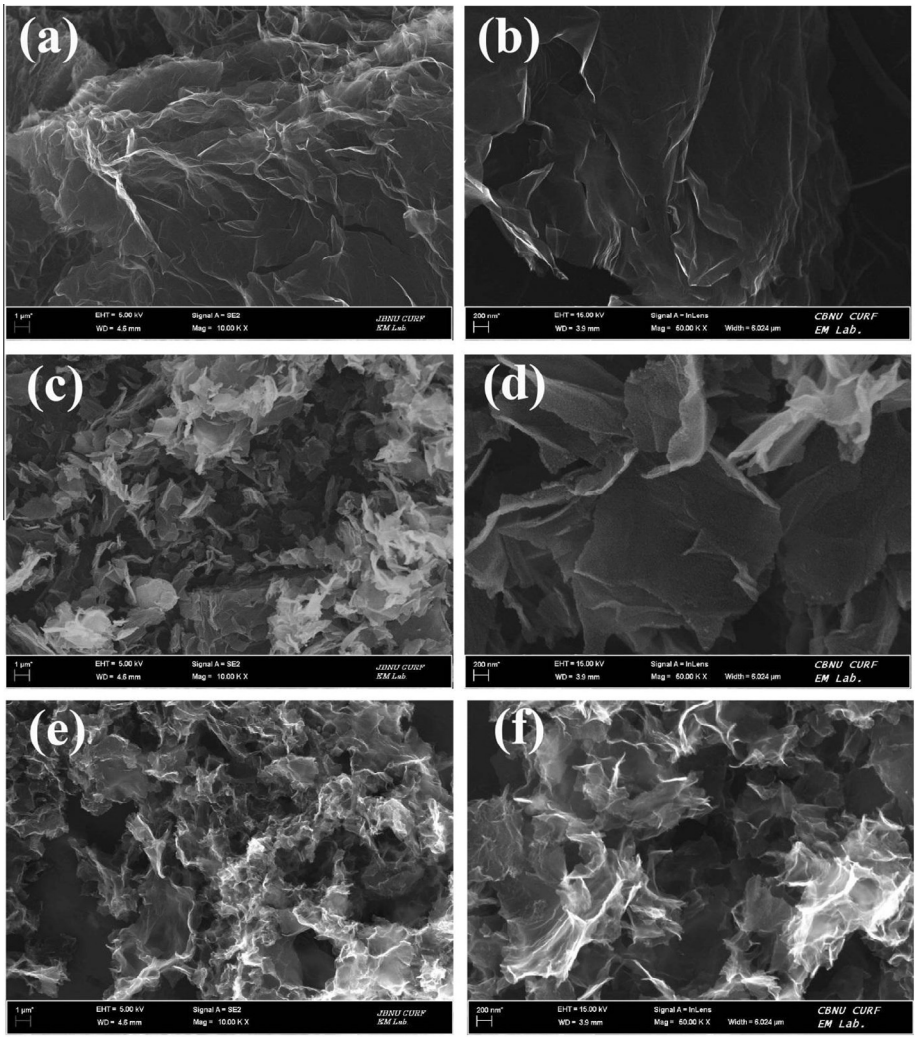

Fig. 7 – SEM images of (a, b) TEG, (c, d) PPD-TEG, and (e, f) NC-TEG.

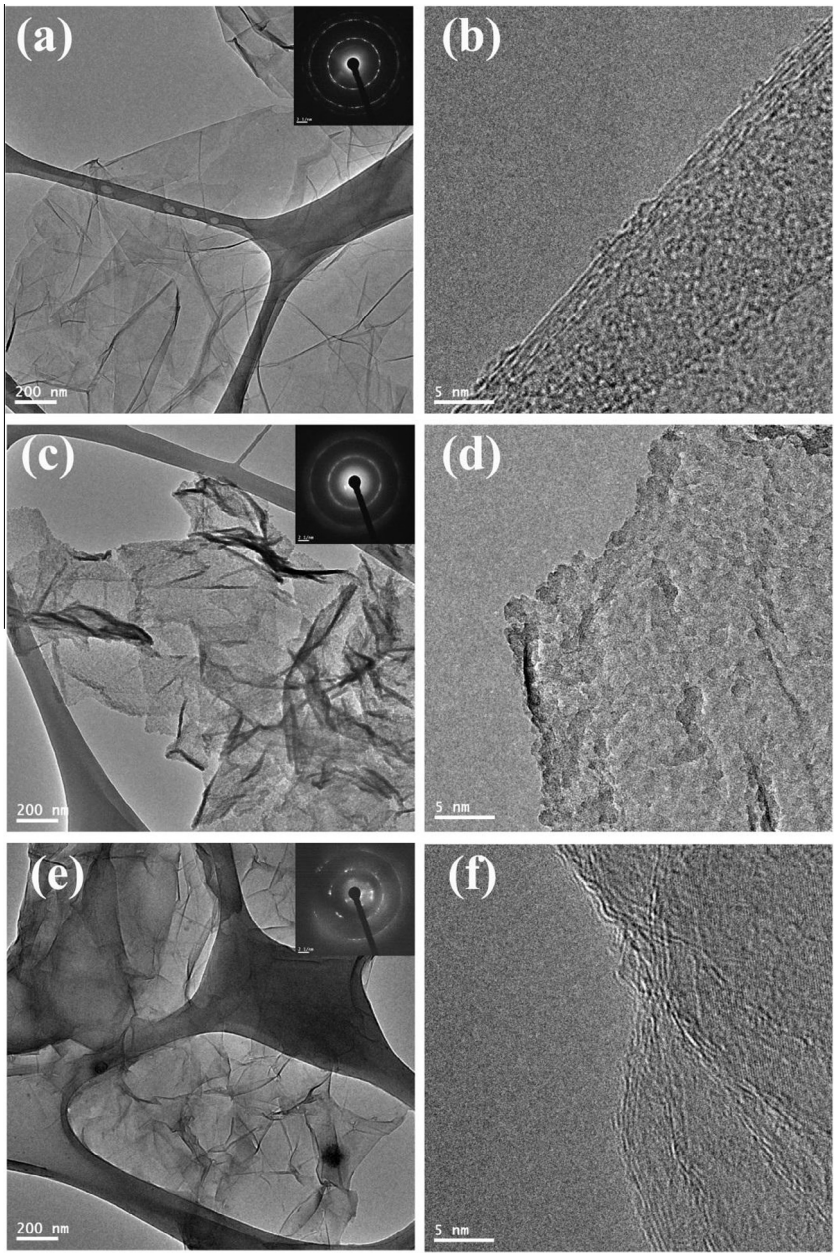

Fig. 8 – TEM images of (a, b) TEG, (c, d) PPD-TEG, and (e, f) NC-TEG.

the composite precursors, the highly aggregated and thick coating morphology was restored within the porous structures. The FE-SEM images at higher magnification showed the existence of incinerated polymer residues along with the TEG flakes [41]. The intrinsic TEG smooth flake surface was partly exposed, while it is posited that the rough part was functionalized with hetero-atom nitrogen-containing carbon structures. The appearance of this kind of surface morphology is an indication of improvement in surface area and capacitive performance.

3.7. *TEM image analysis*

TEM images of TEG, PPD-TEG, and NC-TEG are shown in Fig. 8. TEG showed a transparent and silk veil-like morphology of graphene sheets. The SAED pattern of TEG is shown in the inset of Fig. 8(a). The diffraction spots confirm the crystalline structure of TEG and reveal a few overlapping-layers of graphene sheets. This observation is in good agreement with the observation of FE-SEM image analysis. A high-resolution TEM (HR-TEM) image of TEG edges provides the cross-sectional view shown in Fig. 8(b). The appearance of lattice fringes clearly illustrates the formation of the highly crystalline TEG layer. The TEM images of PPD coated onto TEG surfaces is shown in Fig. 8(c), which shows that that graphene flakes were wrapped with PPD all over surfaces and the folded part of graphene was filled with PPD polymer and demonstrated dark stripes. The SAED pattern of PPD-TEG displayed halo-like circles, confirming the existence of an amorphous composite state. The edge of PPD-coated graphene composite

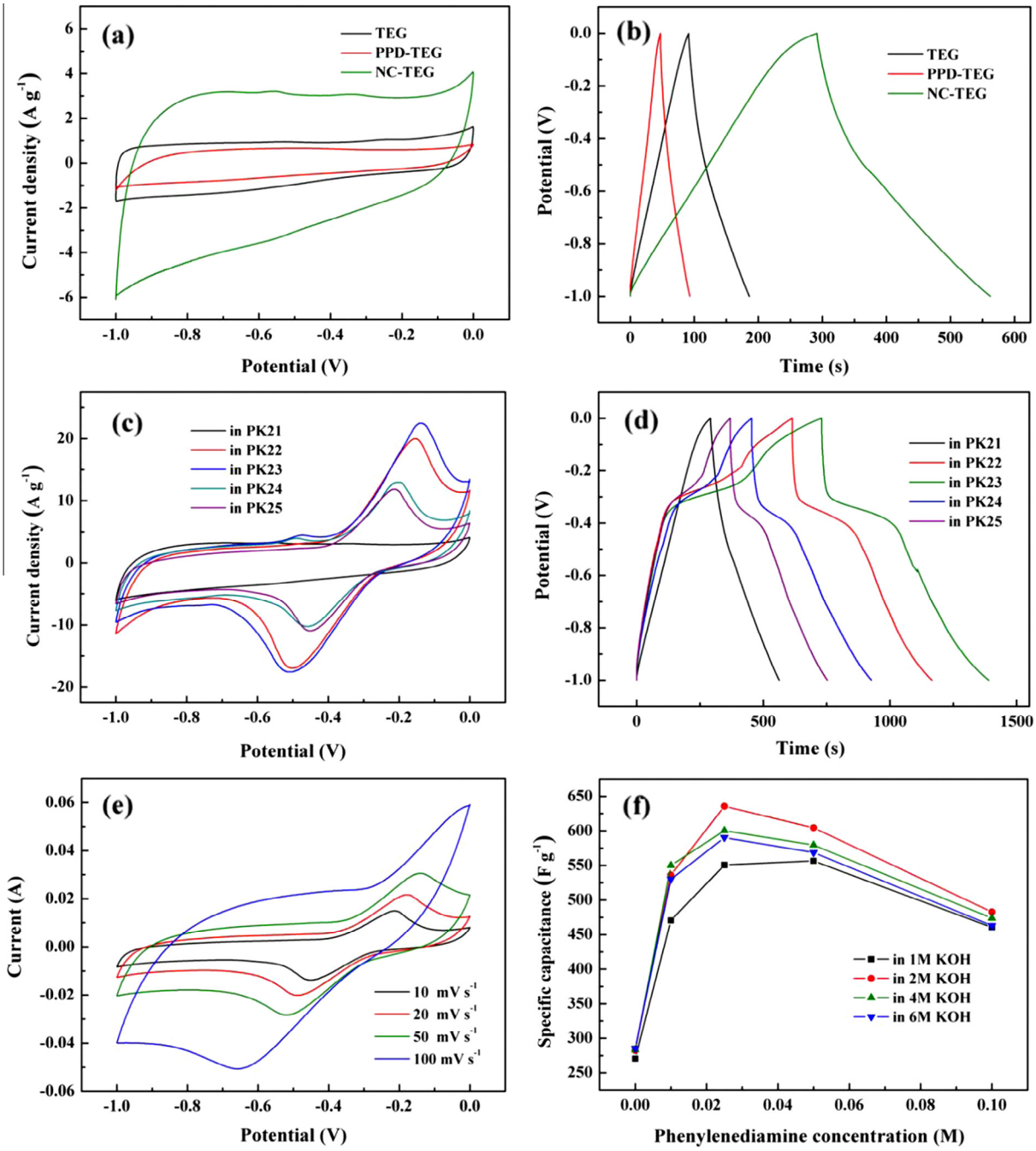

Fig. 9 – (a) CV curves of TEG, PPD-TEG, and NC-TEG, (b) galvanic charge–discharge of TEG, PPD-TEG, and NC-TEG, (c) cyclic voltammetry curves, and (d) galvanic charge–discharge of NC-TEG electrode in different PPD mediator concentrations in 2 M KOH, (e) different scan rates at 2 M KOH with 0.025 M PPD as the electrolyte, (f) the capacitance in different electrolytes. (A colour version of this figure can be viewed online.)

was observed from the HR-TEM images shown in Fig. 8(d). There was no crystalline edge, but only an amorphous rough polymer surface. Moreover, an irregular polymer granule was obtained, which is in good agreement with the FE-SEM image observations. Fig. 8(e) displays the TEM image of NC-TEG and is quite different from that of the PPD-TEG, showing transparent and veil-like flakes due to the decomposition of unstable polymer during annealing at 600 °C. The existence of wrinkles in NC-TEG was stronger than that of pristine TEG due to the increased surface area of NC-TEG. The SAED pattern shown in Fig. 8(f) was partly exposed after incineration, indicating the incomplete carbonization process under 600 °C. The cross-section of the HR-TEM image displayed the multiple edges of NC-TEG flakes created by the carbonization of poly (p-phenylene diamine).

3.8. *Electrochemical study*

Fig. 9(a) shows the electrochemical performance of TEG, PPD-TEG, and NC-TEG characterized in a three-electrode system

using a PK21 electrolyte, operating at a scan rate of 10 mV s^{-1}. The CV plot of the supporting nickel foam electrode exhibits a horizontal linear shape, showing negligible specific capacitance. Near-rectangular CV curves were observed in the TEG and NC-TEG plot. In contrast, the nature of the CV curve of PPD-TEG was sharper and narrower. The maximum current density was recorded in NC-TEG, and its corresponding capacitance reached 283.5 F g^{-1}. The specific capacitances of TEG and PPD-TEG were found to be 92.5 and 52.1 F g^{-1}, respectively. The increased capacitive performance in NC-TEG was attributed to the hetero-atom (nitrogen) doping and the enhanced surface area in the carbonized porous structure augmenting the interface between electrode and electrolyte. The specific capacitance was also calculated via galvanostatic charge–discharge measurements at the current density of 1 A g^{-1}, and the results are shown in Fig. 9(b). The charge–discharge curves of TEG have an isosceles triangle shape, reflecting a steady and symmetrical charging–discharging process. It is noted that the charge–discharge time cycles became shorter for PPD-TEG, which may be attributed to the coating of PPD polymer onto the TEG surfaces resulting in decreased specific surface areas of PPD-TEG. In contrast, the charge–discharge cycle time of NC-TEG was significantly higher than that of TEG or PPD-TEG. It is also noted that the charge–discharge curves were altered slightly due to the pseudo-capacitive effect of faradic reactions caused by the presence of doped nitrogen atoms [42]. Fig. 9(c) shows the CV curves of NC-TEG electrodes in PK21, PK22, PK23, PK24, and PK25 electrolytes. The curves were nearly rectangular shaped in pure KOH (PK21) electrolytes. In contrast, the prominent redox peaks appeared in the CV curves (at −0.2 and −0.5 V) of NC-TEG studied in mixed electrolyte, reflecting pseudo-capacitive behavior due to the reversible electron transfer between the electrolyte and electrodes. The proposed electron transfer mechanism during the redox reaction is illustrated in Fig. 1.

The specific capacitance of NC-TEG calculated from the CV in PK21 electrolyte was found to be ~283 F g^{-1}. The specific capacitance was increased to 536 F g^{-1} in PK22 electrolyte. The specific capacitance was found to increase continuously with the gradual addition of PPD and reached a maximum (635 F g^{-1}) in PK23. Beyond this concentration, the specific capacitance values decreased to 604 and 483 F g^{-1} for PK24 and PK25 electrolytes, respectively. The charge–discharge curves in different electrolytes are also shown in Fig. 9(d). The charge–discharge curves in PK21 (pure KOH solution) show a typical isosceles triangle shape. Interestingly, the charge–discharge curves had a supplementary shoulder due to the pseudo-capacitance had the electron transfer between aromatic di-amine and quinine-imine.

The N-doped elements in the carbon honeycomb structures such as Pyridic N, Pyrrolic N, and Pyridon-N induced pseudo-capacitance greatly under the reaction in alkaline electrolyte [43,44]. The CV curves of NC-TEG in PK23 were tested in different scan rates and are shown in Fig. 9(e). The current density increased gradually with scan rate, indicating a surface-confined electrochemical process [45]. The symmetry redox oxidation reduction shape was maintained without severe distortion up to a scan rate of 50 mV s^{-1}. However, above a 100 mV s^{-1} scan rate, there was a distortion of original symmetry indicating that the electrochemical process is no longer a completely reversible reaction for the pseudo-capacitive electron transfer. The specific capacitance of the NC-TEG electrode in mixed electrolyte (the composition shown in Table 1) was calculated from the cyclic voltammetry experiment, as shown in Fig. 9(f). The highest specific capacitance was achieved in PK23 electrolyte. Over-concentrated mediator restrained capacitive behavior, which was reflected by the decreased capacitive performance when using 0.05 and 0.1 M PPD mediator in the electrolyte. The specific capacitance obtained from the rate capability test decreased with an increase of the current density as shown in the Supporting information (Fig. S1). The Coulombic efficiency shows higher values at high current density than that at low current density of 1 A g^{-1}.

The representative Nyquist plots of NC-TEG with different concentrations of electrolyte consisted of semicircles and straight lines, as shown in Fig. 10(a). The semicircle in the high-frequency region reflects high charge transfer resistance between the electrolyte and electrode surfaces. The straight line in the low-frequency region demonstrated enhanced capacitive performance and low diffusion resistance of ions [46]. The R_{ct} values recorded in PK21, PK22, PK23, PK24 and PK25 (0, 0.01, 0.025, 0.05, and 0.1 M PPD) were found to be 0.23, 0.26, 1.21, 3.15, and 5.32 Ω, respectively. The R_L (liquid

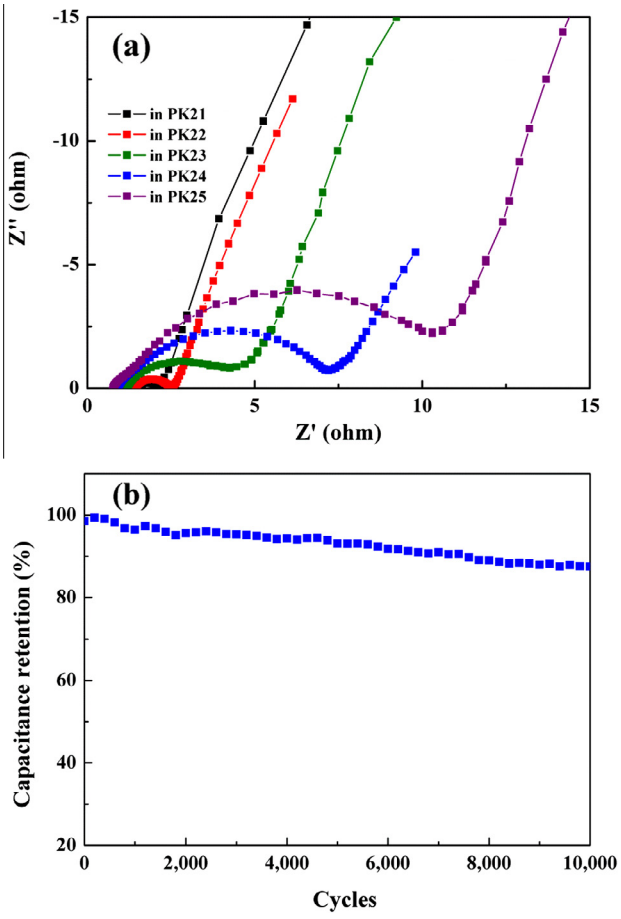

Fig. 10 – (a) EIS spectrum of NC-TEG with altered PPD concentrations, and (b) capacitance retention of NC-TEG (2 M KOH with 0.025 M PPD). (A colour version of this figure can be viewed online.)

resistance) values in PK21, PK22, PK23, PK24, and PK25 were found to be 0.74, 0.95, 1.21, 1.43, and 1.47 Ω, respectively. These results indicate that PPD is ameliorating the contact between the electrolyte and electrode materials. Fig. 10(b) shows the electrochemical stability of NC-TEG electrodes up to 5000 charge–discharge cycles. There was a minor fluctuation initially, followed by relative stability in the subsequent cycles. Retention of specific capacitance for NC-TEG was ~87.4% after 10,000 charge–discharge cycles.

4. Conclusion

NC-TEG was successfully prepared by a two-step procedure, polymerization of PD with TEG and subsequent pyrolysis. FTIR spectrum and X-ray photoelectron analyses showed changes in the chemical composition of PPD-TEG precursor and NC-TEG, and SEM and TEM monitored the alteration in morphology after carbonization. Physisorption analysis showed that NC-TEG samples have not only enlarged surface areas, but also improved hierarchical 3D structures richer in micro-pores and meso-pores than pristine TEG. Compared with TEG, the specific capacitance of NC-TEG electrodes increased to 282.5 F g^{-1}. Moreover, PD acted as a faradaic transfer agent by increasing the capacitive behavior. Cyclic voltammetry and galvanic charge–discharge tests revealed that the EDLC effect of NC-TEG cooperates with the pseudo-capacitive behavior of the electrolyte mediator. The specific capacitance of NC-TEG was increased significantly from 282.5 F g^{-1} (2 M KOH) to 635.6 F g^{-1} (2 M KOH, 0.025 M PPD). The EIS result shows that the PD mediator affects the supercapacitor internal resistance but ameliorates the problem of electrolyte and electrode contact. The capacitive retention shows remarkable stability as high as 87.4% after 10,000 cycles.

Acknowledgements

This study was supported by the Converging Research Center Program (2014M3C1A8048834) and the Basic Research Laboratory Program (2014R1A4A1008140) through the Ministry of Science, ICT & Future Planning and by the Basic Science Research Program through the National Research Foundation (NRF) funded by the Ministry of Education of Korea (2013R1A1A2011608).

Appendix A. Supplementary data

Supplementary data associated with this article can be found, in the online version, at http://dx.doi.org/10.1016/j.carbon.2014.12.069.

REFERENCES

[1] Simon P, Gogotsi Y. Materials for electrochemical capacitors. Nat Mater 2008;7(11):845–54.
[2] Qu DY, Shi H. Studies of activated carbons used in double-layer capacitors. J Power Sources 1998;74(1):99–107.
[3] Xiong SX, Yang F, Jiang H, Ma J, Lu XH. Covalently bonded polyaniline/fullerene hybrids with coral-like morphology for high-performance supercapacitor. Electrochim Acta 2012;85:235–42.
[4] Pech D, Brunet M, Durou H, Huang PH, Mochalin V, Gogotsi Y, et al. Ultrahigh-power micrometre-sized supercapacitors based on onion-like carbon. Nat Nanotechnol 2010;5(9):651–4.
[5] Frackowiak E, Metenier K, Bertagna V, Beguin F. Supercapacitor electrodes from multiwalled carbon nanotubes. Appl Phys Lett 2000;77(15):2421–3.
[6] Kim C, Yang KS. Electrochemical properties of carbon nanofiber web as an electrode for supercapacitor prepared by electrospinning. Appl Phys Lett 2003;83(6):1216–8.
[7] Zhang K, Ang BT, Zhang LL, Zhao XS, Wu JS. Pyrolyzed graphene oxide/resorcinol-formaldehyde resin composites as high-performance supercapacitor electrodes. J Mater Chem 2011;21(8):2663–70.
[8] Li X-G, Li A, Huang M-R, Liao Y, Lu Y-G. Efficient and scalable synthesis of pure polypyrrole nanoparticles applicable for advanced nanocomposites and carbon nanoparticles. J Phys Chem C 2010;114(45):19244–55.
[9] Bose S, Kuila T, Mishra AK, Rajasekar R, Kim NH, Lee JH. Carbon-based nanostructured materials and their composites as supercapacitor electrodes. J Mater Chem 2012;22(3):767–84.
[10] Geim AK, Novoselov KS. The rise of graphene. Nat Mater 2007;6(3):183–91.
[11] McAllister MJ, Li J-L, Adamson DH, Schniepp HC, Abdala AA, Liu J, et al. Single sheet functionalized graphene by oxidation and thermal expansion of graphite. Chem Mater 2007;19(18):4396–404.
[12] Yan YN, Kuila T, Kim NH, Ku B-C, Lee JH. Effects of reduction and polystyrene sulfate functionalization on the capacitive behaviour of thermally exfoliated graphene. J Mater Chem A 2013;1(19):5892–901.
[13] Lv W, Tang DM, He YB, You CH, Shi ZQ, Chen XC, et al. Low-temperature exfoliated graphenes: vacuum-promoted exfoliation and electrochemical energy storage. ACS Nano 2009;3(11):3730–6.
[14] Zhang HB, Wang JW, Yan Q, Zheng WG, Chen C, Yu ZZ. Vacuum-assisted synthesis of graphene from thermal exfoliation and reduction of graphite oxide. J Mater Chem 2011;21(14):5392–7.
[15] Zhu Y, Murali S, Stoller MD, Ganesh KJ, Cai W, Ferreira PJ, et al. Carbon-based supercapacitors produced by activation of graphene. Science 2011;332(6037):1537–41.
[16] Poh HL, Simek P, Sofer Z, Tomandl I, Pumera M. Boron and nitrogen doping of graphene via thermal exfoliation of graphite oxide in a BF_3 or NH_3 atmosphere: contrasting properties. J Mater Chem A 2013;1(42):13146–53.
[17] Poh HL, Simek P, Sofer Z, Pumera M. Sulfur-doped graphene via thermal exfoliation of graphite oxide in H_2S, SO_2, or CS_2 gas. ACS Nano 2013;7(6):5262–72.
[18] Hasan SA, Tsekoura EK, Sternhagen V, Stromme M. Evolution of the composition and suspension performance of nitrogen-doped graphene. J Phys Chem C 2012;116(11):6530–6.
[19] Sun L, Wang L, Tian C, Tan T, Xie Y, Shi K, et al. Nitrogen-doped graphene with high nitrogen level via a one-step hydrothermal reaction of graphene oxide with urea for superior capacitive energy storage. RSC Adv 2012;2(10):4498–506.
[20] Yang JH, Yang GZ, Yu DG, Wang X, Zhao B, Zhang LL, et al. Carbon foams from polyacrylonitrile borneol films prepared using coaxial electro-hydrodynamic atomization. Carbon 2013;53:231–6.
[21] Mizuno T, Takizawa M, Tsuchiya B, Jinno M, Bandow S. A nitrogen-doped graphene film prepared by chemical vapor

deposition of a methanol mist containing methylated melamine resin. Appl Phys A-Mater 2013;113(3):645–50.
[22] An B, Xu S, Li L, Tao J, Huang F, Geng X. Carbon nanotubes coated with a nitrogen-doped carbon layer and its enhanced electrochemical capacitance. J Mater Chem A 2013;1(24):7222–8.
[23] Lee JY, Liang K, An KH, Lee YH. Nickel oxide/carbon nanotubes nanocomposite for electrochemical capacitance. Synth Met 2005;150(2):153–7.
[24] Cheng Q, Tang J, Ma J, Zhang H, Shinya N, Qin L-C. Graphene and nanostructured MnO_2 composite electrodes for supercapacitors. Carbon 2011;49(9):2917–25.
[25] Wu ZS, Wang DW, Ren W, Zhao J, Zhou G, Li F, et al. Anchoring hydrous RuO_2 on graphene sheets for high-performance electrochemical capacitors. Adv Funct Mater 2010;20(20):3595–602.
[26] Roldan S, González Z, Blanco C, Granda M, Menéndez R, Santamaría R. Redox-active electrolyte for carbon nanotube-based electric double layer capacitors. Electrochim Acta 2011;56(9):3401–5.
[27] Roldan S, Granda M, Menéndez R, Santamaría R, Blanco C. Mechanisms of energy storage in carbon-based supercapacitors modified with a quinoid redox-active electrolyte. J Phys Chem C 2011;115(35):17606–11.
[28] Su LH, Zhang XG, Mi C-H, Gao B, Liu Y. Improvement of the capacitive performances for Co-Al layered double hydroxide by adding hexacyanoferrate into the electrolyte. Phys Chem Chem Phys 2009;11(13):2195–202.
[29] Granda M, Roldán S, Menéndez R, Santamaría R, Blanco C. Supercapacitor modified with methylene blue as redox active electrolyte. Electrochim Acta 2012;83:241–6.
[30] Lota G, Milczarek G. The effect of lignosulfonates as electrolyte additives on the electrochemical performance of supercapacitors. Electrochem Commun 2011;13(5):470–3.
[31] Yu H, Wu J, Fan L, Lin Y, Xu K, Tang Z, et al. A novel redox-mediated gel polymer electrolyte for high-performance supercapacitor. J Power Sources 2012;198:402–7.
[32] Yu H, Wu J, Fan L, Xu K, Zhong X, Lin Y, et al. Improvement of the performance for quasi-solid-state supercapacitor by using PVA–KOH–KI polymer gel electrolyte. Electrochim Acta 2011;56(20):6881–6.
[33] Ke NJ, Lu S-S, Cheng S-H. A strategy for the determination of dopamine at a bare glassy carbon electrode: p-phenylenediamine as a nucleophile. Electrochem Commun 2006;8(9):1514–20.
[34] Khan IM, Ahmad A. Synthesis, spectrophotometric, structural and thermal studies of the charge transfer complex of p-phenylenediamine, as an electron donor with π acceptor 3,5-dinitrobenzoic acid. Spectrochim Acta A: Mol Biomol Spectrosc 2010;76(3–4):315–21.
[35] Wu J, Yu H, Fan L, Luo G, Lin J, Huang M. A simple and high-effective electrolyte mediated with p-phenylenediamine for supercapacitor. J Mater Chem 2012;22(36):19025–30.
[36] Chen CM, Zhang Q, Yang MG, Huang CH, Yang YG, Wang MZ. Structural evolution during annealing of thermally reduced graphene nanosheets for application in supercapacitors. Carbon 2012;50(10):3572–84.
[37] Li Y, Li T, Yao M, Liu S. Metal-free nitrogen-doped hollow carbon spheres synthesized by thermal treatment of poly (o-phenylenediamine) for oxygen reduction reaction in direct methanol fuel cell applications. J Mater Chem 2012;22(21):10911–7.
[38] Plachy T, Sedlacik M, Pavlinek V, Moravkova Z, Hajna M, Stejskal J. An effect of carbonization on the electrorheology of poly (p-phenylenediamine). Carbon 2013;63:187–95.
[39] Zhu H, Wang X, Liu X, Yang X. Integrated synthesis of poly(o-phenylenediamine) derived carbon materials for high performance supercapacitors. Adv Mater 2012;24(48):6524–9.
[40] Li J, Xie H, Li Y, Liu J, Li Z. Electrochemical properties of graphene nanosheets/polyaniline nanofibers composites as electrode for supercapacitors. J Power Sources 2011;196(24):10775–81.
[41] Zhang K, Ang BT, Zhang LL, Zhao XS, Wu J. Pyrolyzed graphene oxide/resorcinol-formaldehyde resin composites as high-performance supercapacitor electrodes. J Mater Chem 2011;21(8):2663–70.
[42] Wei L, Sevilla M, Fuertes AB, Mokaya R, Yushin G. Polypyrrole-derived activated carbons for high-performance electrical double-layer capacitors with ionic liquid electrolyte. Adv Funct Mater 2012;22(4):827–34.
[43] Lee YH, Chang KH, Hu CC. Differentiate the pseudocapacitance and double-layer capacitance contributions for nitrogen-doped reduced graphene oxide in acidic and alkaline electrolytes. J Power Sources 2013;227:300–8.
[44] Zhang H, Kuila T, Kim NH, Yu DS, Lee JH. Simultaneous reduction, exfoliation, and nitrogen doping of graphene oxide via a hydrothermal reaction for energy storage electrode materials. Carbon 2014;69:66–78.
[45] Kuila T, Mishra AK, Khanra P, Kim NH, Uddin ME, Lee JH. Facile method for the preparation of water dispersible graphene using sulfonated poly(ether–ether–ketone) and its application as energy storage materials. Langmuir 2012;28(25):9825–33.
[46] Kuila T, Khanra P, Kim NH, Lim JK, Lee JH. Effects of sodium hydroxide on the yield and electrochemical performance of sulfonated poly (ether-ether-ketone) functionalized graphene. J Mater Chem A 2013;1(32):9294–302.